A Semi-automatic 3D mesh segmentation based on Cross-Boundary strokes

Jiguang Lian[1], Haisheng Li[1], Nan Li[1], and Xiaochuan Wang[1]

[1]Beijing Technology and Business University

December 2, 2022

Abstract

3D segmentation has been a hot spot in numerical geometry processing. But the accuracy of the segmentation methods can be easily affected by the types of models because their sensitivity to different models is uneven. To address this problem, we propose a semi-automatic 3D mesh segmentation algorithm based on harmonic field. Firstly, our algorithm utilizes the strokes of users as constraints on the harmonic field of the mesh surface. Secondly, a smooth harmonic field based on Laplacian operator and Poisson equation is introduced. Through the generated harmonic field, the correct weights are selected to further fit the geometric characteristics of the grid. Afterwards, we find a set of most suitable isolines on the harmonic field as the segmentation path. Finally, a mesh density enhancement method is designed, which optimizes sub-graphs after segmentation. Experimental results demonstrate that the effectiveness of our proposed algorithm. Moreover, the semi-automatic 3D mesh segmentation algorithm can better understand the intention of users.

figures/fig1-The-pipeline-of-the-proposed-method/fig1-The-pipeline-of-the-proposed-method figures/fig2-The-line-segments-identified-by-the-user/fig2-The-line-segments-identified-b figures/fig3-Harmonic-field-color-change-diagram/fig3-Harmonic-field-color-change-diagram figures/fig4-The-isolines-generated-on-the-mesh/fig4-The-isolines-generated-on-the-mesh-e figures/fig5-The-segmention-effect-of-the-selected-isoline/fig5-The-segmention-effect-of-figures/fig6-Schematic-diagram-of-isoline-crossing-boundary/fig6-Schematic-diagram-of-isol figures/fig7-Comparison-diagram-before-and-after-optimization-aBefore-optimization-bAfter figures/fig8-The-Segmentation-results-of-bear-model-based-on-the-8th-segmentation-line/fi figures/fig9-The-segmentation-results-of-our-method-on-the-basis-of-isoline-selection-expe figures/fig10--The-results-of-multi-component-segmentation/fig10--The-results-of-multi-co figures/fig11-The-results-of-binary-segmentation/fig11-The-results-of-binary-segmentation-figures/fig12-Comparison-of-boundary-optimization,-the-right-figure-shows-the-optimized-r figures/fig13-Comparison-of-segmentation-results-with-two-other-methods/fig13-Comparison-figures/fig14-Comparison-of-segmentation-results-with-two-other-methods-on-human-model/fi figures/fig15-The-quantitative-comparison-evaluation-of-the-proposed-method,-the-last-col

A Semi-automatic 3D mesh segmentation based on Cross-Boundary strokes

Jiguang Lian[a,b,c], Haisheng Li[a,b,c,1,*], Nan Li[a], Xiaochuan Wang[a]

[a]*Beijing Technology and Business University, , Beijing, 100048, , China*
[b]*Beijing Key Laboratory of Big Data Technology for Food Safety, , Beijing, 100048, , China*
[c]*National Engineering Laboratory For Agri-product Quality Traceability, , Beijing, 100048, , China*

Abstract

3D segmentation has been a hot spot in numerical geometry processing. But the accuracy of the segmentation methods can be easily affected by the types of models because their sensitivity to different models is uneven. To address this problem, we propose a semi-automatic 3D mesh segmentation algorithm based on harmonic field. Firstly, our algorithm utilizes the strokes of users as constraints on the harmonic field of the mesh surface. Secondly, a smooth harmonic field based on Laplacian operator and Poisson equation is introduced. Through the generated harmonic field, the correct weights are selected to further fit the geometric characteristics of the grid. Afterwards, we find a set of most suitable isolines on the harmonic field as the segmentation path. Finally, a mesh density enhancement method is designed, which optimizes sub-graphs after segmentation. Experimental results demonstrate that the effectiveness of our proposed algorithm. Moreover, the semi-automatic 3D mesh segmentation algorithm can better understand the intention of users.

Keywords: 3D segmentation, Semantic segmentation, Isolines constraint, Harmonic field, User interaction

*Corresponding author

Email addresses: 2304273008@qq.com (Jiguang Lian), lihsh@btbu.edu.cn (Haisheng Li), linan@th.btbu.edu.cn (Nan Li), wangxc@btbu.edu.cn (Xiaochuan Wang)

1. Introduction

In geometric processing and shape understanding, 3D object segmenting is a fundamental problem. It performs an important role in assisting parametrization, texture mapping Sander et al. [1], shape matching, 3D shape modelling [2], 3D model generation Li et al. [3], animation [4], mesh parameterization [5, 6], 3D models feature matching [7], deformation [8, 9], 3D object retrieval [10, 11, 12], compression [13], etc. Mesh segmentation aims to decompose a mesh, representing a 3D object, into parts.

Mesh segmentation methods can be divided into two categories: part-type.(or semantic) [14] and surface-type [15, 16, 17] methods. In terms of part-type segmentation [18], the goal is to segment the object represented by the mesh into meaningful, mostly volumetric, parts. In surface-type segmentation, the objective is to segment the surface mesh into patches under some criteria. The former pays more attention to the geometric information of the mesh to obtain the surfaces constituting the original object, which is suitable for texture mapping, etc. In the latter case, the algorithms are greatly based on the human perception theory to segment the mesh model into meaningful parts. It is important to find the human vision that delineates the boundaries of object's regions along the negative minima of principal curvatures. Lee et al. [19, 20] found the region boundaries using the shortest path between two vertices that satisfies a specific cost function. Hou et al. [21] introduced a novel region fusion algorithm which is able to handle 3D meshes with complex shape and rich details. Most of existing methods need explicit information on segmentation boundary and the above methods are automatic segmentation, however, the results of segmentation also often depend on the specific application, so a fully automatic segmentation algorithm is not realistic, and the mesh has to be segmented through user interaction depending on the actual application.

Meanwhile, the accuracy of existing methods is easily affected by the types of models, and their sensitivity to different models is uneven. Semantic segmentation remains a challenge. Currently, user need referred segmentation technology for a specific semantic component (such as the head, extremities and tail) is still immature.

Therefore, we study the semantic information of the mesh based on the requirements of users. Since the harmonic field is a continuous and smooth scalar field, applying it to the mesh surface can meet the requirements of semi-automatic mesh segmentation. By using the users' stroke as the segmentation constraint, a smooth harmonic field tone is introduced to capture the user's intention to generate a set of isolines. Through the selection of weight, the generated harmonic field is more in line with the geometric characteristics of the mesh itself, and the most suitable isoline is selected as the segmentation path. Finally, the segmentation path is optimized.

2. Related Works

2D image segmentation is the basis of 3D model segmentation. Fuzzy local intensity clustering is used to achieve automatic medical image segmentation [22]. [23] Combining the point-wise features and global point features [20], the semantic information is obtained. In order to promote the accuracy of whole brain segmentation, Chen et al. [24] make full use of the spatial constraint information between adjacent slice of magnetic resonance imaging brain image sequence. On the basis of 2D image segmentation, the segmentation of the 3D mesh model has become one important stage in the area of mesh processing. In some previous work, mesh segmentation primarily extend image segmentation algorithm, mesh simplification, mesh feature extraction and other technologies, in order to separate the mesh according to the extracted information, However, present mesh segmentation increasingly more attention to the semantic part.

Recently, many semantic segmentation methods have been adopted in graphic processing. In 2015, Jia et al. [25] introduced curvature extreme points into the segmented fuzzy region to achieve watershed segmentation by pre segmenting the mesh. Garland et al. [26] proposed a hierarchical clustering algorithm based on mesh patches. Its idea is to merge adjacent triangular patches into sub clusters, continuously shrinking and simplifying the clustering seeds, and achieve the clustering of all patches. Sander et al. [1] proposed an iterative approach for mesh segmentation based on K-means. Lian et al. [27] achieve one adaptive mesh segmentation is implemented interactively according to the user's requirements. Subsequently, David et al. [28] achieved the similarity measurement of face pieces based on the variational shape approximation method. Fang et al. [29] used the heat kernel perception on the mesh to obtain global information fand automatically implement segmentation. Yang et al. [30] achieved good results by using persistent clustering and wave kernel features. At present, spectral clustering method has attracted much attention. It maps the three-dimensional mesh information to the spectral space and uses the feature vector to cluster to achieve mesh segmentation. Wang et al. [31] used the Laplace operator to obtain the connected single sub mesh region, Chahhou et al. [32] used adjacency distance measurement minimization to extract the sub-segmented region, and Yang et al. [33] optimized the Laplacian matrix to recognize the model attitude on the mesh. In 2018, Tong et al. [34] introduced gradient minimization into the mesh segmentation, mapping the mesh segmentation to constant vectors.

Recently, Moon et al. [35] present a new method for interactive segmentation of a triangle mesh by using the concavity-sensitive harmonic field and anisotropic geodesic. The proposed method only requires a single vertex in the desired feature region, while the vertex is not easily selected by user click. Meanwhile, the segmentation boundary is constructed by computing anisotropic geodesics passing through the interpolation points. However, this will result in a non-smooth segmentation boundary. In this paper, we carry out local division of the sub-mesh on the original mesh involved in order to ensure the quality of the smooth boundary.

3. Methodology

This section presents the semi-automatic 3D mesh segmentation algorithm based on Cross-Boundary strokes. First, user interaction is performed to generate strokes. Then the harmonic field of the mesh surface is constructed by combining the mesh geometric information. Afterwards a set of isoline lines is formed by using the scalar field values generated by the harmonic field and select the best isoline selected as the segmentation path. Finally, the results are optimized by local mesh density enhancement. Fig.1 shows the pipeline of our method.

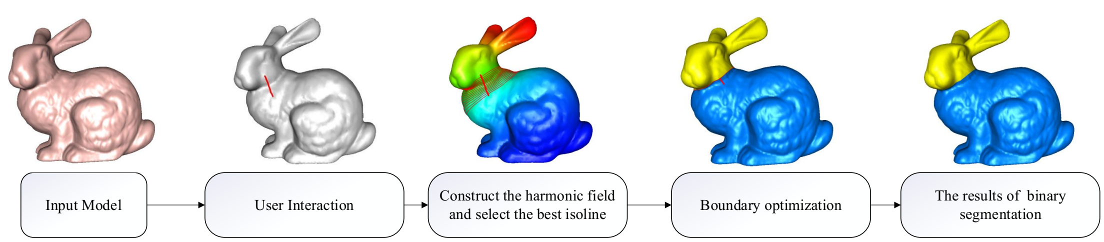

Figure 1: The pipeline of the proposed method.

3.1. Harmonic Field construction

3.1.1. Interactive harmonic field

To achieve the semi-automatic 3D mesh segmentation combined with the user intention, it is necessary to introduce interaction. The harmonic field is just a continuous and smooth scalar field, which is characterized by passivity, non-rotational and non-local extremum. When acting on the mesh surface, it may well meet the requirements of mesh deformation, quadrilateral and semi-automatic mesh segmentation. For this reason, we should initially construct the harmonic field on the mesh surface.

First construct a scalar function $u\colon \mathbf{V} \to \mathbf{R}$, which defines the corresponding scalar value at all mesh points. By linear interpolation on each triangular slice this function is generalized to define a slice linear function on the entire mesh. Secondly, it is specified that the line segment identified by the user on the mesh surface is a directed line segment, which has the same function as identifying the foreground and background in image segmentation and extracting the subject image. The segment identified by the user are illustrated in Fig.2.

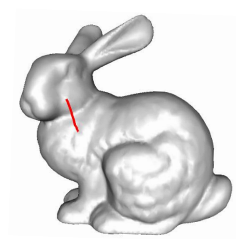

Figure 2: The line segments identified by the user.

Let $P = \{p_1, p_2, \cdots p_c\}$ and $Q = \{q_1, q_2, \cdots q_c\}$ represent the corresponding set of mesh vertex indexes at the beginning and end of line segments respectively, where c is the number of strokes. Our method introduces the Poisson equation:

$$\Delta u = 0 \tag{1}$$

In particular, we are focused on the construction of the harmonic function u, which satisfies the Laplace equation corresponding to a specific Dirichlet boundary condition. Combined with the Dirichlet constraints:

$$E_1 = \begin{cases} u_x = 1, & x \epsilon P \\ u_x = 0, & x \epsilon Q \end{cases} \tag{2}$$

where u satisfying the above Dirichlet constraints is a discrete harmonic function and Δ is a Laplace operator with cotangent weighting.

The Poisson equation can be solved in least squares sense by applying the matrix form $\mathbf{Au} = b$, with:

$$\mathbf{A} = \begin{bmatrix} \mathbf{L} \\ \mathbf{WP} \end{bmatrix} \text{and}\, b = \begin{bmatrix} \mathbf{0} \\ \mathbf{WB} \end{bmatrix} \tag{3}$$

where $\mathbf{L}$ is the cotangent Laplacian matrix, $\mathbf{W}$ is positional weighting matrix, $\mathbf{P}$ is the positional matrix of size $2c \times n$, with n denoting the number of mesh vertices, and $\mathbf{B}$ is a $2c \times 1$ matrix solving the solution of Poisson's equation is equivalent to calculating $u = (\mathbf{A}^\top \mathbf{A})^{-1} \mathbf{A}^\top b$.

The Laplace operator on the mesh is commonly expressed as:

$$(\Delta u)_i = \frac{1}{A_i} \sum_{j \epsilon N_i} \omega_{ij} (u_i - u_j) \tag{4}$$

where N_i is the set of neighbor points for the vertex, w_{ij} is the weight corresponding to edge ij and $\sum w_{ij} = 1$, therefore the Laplace equation is discretized into a sparse linear system $\mathbf{Lu} = \mathbf{b}$, where the matrix $\mathbf{L}$ is the discrete Laplace operator matrix. Thus, we obtain the harmonic field generated by the mesh surface, which can achieve that each vertex matches a harmonic field value.

3.1.2. Characteristic reservation

It can be noted that the construction of harmonic function has certain parameters to choose, which also reflects the advantage of semi-automatic segmentation that respects the intention of the user. The parameter as a harmonic function mentioned in the discretization of the Laplace operator mentioned in the Sec.3.1.1 is mainly used to adjust the adaptability of harmonic fields to the mesh. Different harmonic fields and harmonic field values, acting on mesh vertices can be obtained by different parameters.

We introduce discrete cotangent weighting $\omega_{ij} = \frac{1}{2}(\cot \alpha_{ij} + \cot \beta_{ij})$ as here. α_{ij} and β_{ij} are the two angles opposite of the edge ij, by using the characteristics of cotangent weighting, we can represent the local geometric information.

Additionally, we combine various geometrical information and geometric features on the mesh and adopt the weight:

$$\omega_{ij} = \sigma \omega_{ij}^n + (1 - \sigma) \omega_{ij}^c \tag{5}$$

where $\omega_{ij}^n = (1+\frac{\alpha_{ij}}{avg(\alpha_{ij})})^{-1}$, α_{ij} is the angle between the normal vectors $\mathbf{n}_i$ and $\mathbf{n}_j$ of the vertex v_i and v_j, $\omega_{ij}^c = \frac{1}{\sqrt{(|k_n|)+1}}$, $k_n = 2\frac{(\mathbf{v}_i-\mathbf{v}_j)\mathbf{n}^i}{||\mathbf{v}_i-\mathbf{v}_j||^2}$ is approximately the normal curvature on edge ij, σ is the weight between ω_{ij}^n and ω_{ij}^c, which is used to balance the vertex normal angle and normal curvature of the vertex. It is set to 0.5 in most cases.

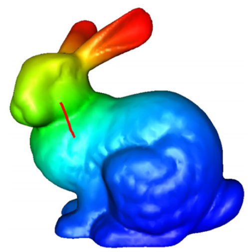

Figure 3: Harmonic field color change diagram.

As shown in Fig.3, the essence of constructing a harmonic field is to construct a set of scalar fields on the mesh, use the smooth nature of the harmonic field, and obtain the harmonic field values on the mesh surface by interpolation on the mesh surface, so as to provide the basis of mathematical theory and practical operation for the subsequent mesh segmentation method using isolines.

3.2. Isoline selection

The construction of harmonic field on the mesh surface allows us to segment the mesh by isoline. The key feature of isoline is that each isoline on the mesh can divide the complete mesh model into two sub mesh models. Additionally, the contour extracted from the interpolated harmonic field is smooth, does not require post-processing, and can even cover the noise on the mesh. Therefore, the present issue is how to select an isoline, in other words, determines an isoline for segmentation combined with user intent and local shape information. Isoline properties based upon the harmonic field include:

(1) Each isoline is a smooth connecting loop, so it is suitable to use directly as division boundary.

(2) The basic harmonic field and the extracted contour are essentially smooth and insensitive to variations in noise, pose, mesh quality and user strokes.

(3)The computational efficiency of isoline selection in harmonic field is high, which only involves solving sparse linear system.

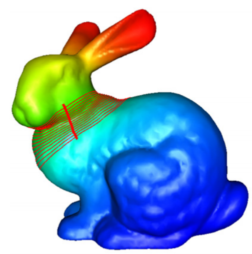

Figure 4: The isolines generated on the mesh.

We uniformly deploy a set of isolines $ISO = \{I_1, I_2, ..., I_N\}$ on the harmonic field generated in the specified interval, and the value of the isoline I_i is $i/(N+1)$. The generated isoline generally runs through the user's scribed line, where N is generally 15. The generated isoline is shown in Fig.4.

Firstly, in order to solve the issue of understanding the intention of the user, we introduce center-ness to measures each isoline of the two ends of the stroke to ensure the best cut should runs across somewhere in the middle of the stroke, but not near its two ends: $Cen_i = e^{-\frac{(i-1)^2}{2t^2}}$, with $t = \frac{N}{2}$. Secondly, the selection of isolines should be combined with local geometry information. More precisely, for each isoline, we first calculate its local radius r_i and divide its length l by 2π. The radius distribution of the isoline assembly represents the change of local volume of the mesh itself, where the radius is the local thickness. Thirdly, we calculate $\Lambda_i = 2r_i - r_{i-1} - r_{i+1}$ for each isoline I_i, where smaller negative Λ_i value represents a larger concave region. In particular, to avoid Λ_i from being zero due to dense isolines, we use $\Lambda_{ik} = 2r_i - r_{i-k} - r_{i+k}$, $k < 1$ to provide a larger step size. In addition, we not only consider adjacent isolines, but use a multi-scale metric Λ_i. In order to penalize isolines of large distances from I_i, we convolute Λ_i with Gaussian function $f(k) = e^{1\frac{(k-1)^2}{2\sigma^2}}$, with σ is 2. The Λ_i is defined as:

$$\Delta_i = \frac{\sum_k f(k)\Delta_{ik}}{\sum_k f(k)} \tag{6}$$

Finally, we combine Λ_i with above-mentioned Cen_i to achieve the final measurement of each isoline:

$$M_i = Cen_i \Lambda_i \tag{7}$$

The isoline with the smallest M_i value is determined as the best segmentation path, as shown in Fig.5.

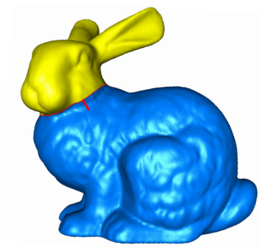

Figure 5: The segmentation effect of the selected isoline.

3.3. Boundary optimization

In the previous section, we obtained the optimal segmentation. When constructing the harmonic field, we use the interpolation method to extend the vertex scalar field to the entire surface mesh scalar field, so as to obtain a smooth harmonic field. However, the subsequent isolines do not necessarily follow the vertices, but cross the mesh edges, as shown in Fig.6. We select the segmentation according to the distance from the vertex to the isoline. In the model with low accuracy, the edges of mesh segmentation may be uneven, and even eliminate the benefits of the above isoline method.

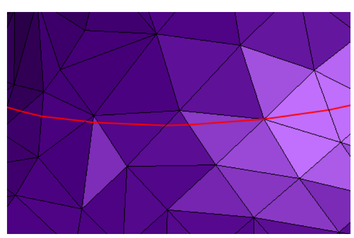

Figure 6: Schematic diagram of isoline crossing boundary.

Therefore, We apply a local subdivision to the submesh on the original mesh. The harmonic field of the submesh can be determined from the original mesh. After selecting the optimal segmentation isoline, we mesh the pre-segmented area to make the mesh itself close to the segmentation path indicated by the contour. There is no change in the harmonic field before and after mesh density enhancement. The following is the energy function after density enhancement E_1 :

$$E_1 = \begin{cases} \overline{u_i}, & x_i = 1 \\ 1 - \overline{u_i}, & x_i = 0 \end{cases} \tag{8}$$

where $\overline{u_i}$ is the average value of harmonic function of each vertex of triangular mesh surface f. Harmonic function E_2:

$$E_2(x_i, x_j) = \eta E_{ang}(f_i, f_j) + (1-\eta) E_{edge}(i, j) \tag{9}$$

where,

$$E_{ang}(f_i, f_j) = (1 + \frac{d_{ang}(f_i, f_j)}{avg(d_{ang}(f_i, f_j))})^{-1} \tag{10}$$

$$d_{ang}(f_i, f_j) = 1 - \cos(\alpha_{ij}) \tag{11}$$

where α_{ij} is dihedral angle, $E_{edge}(i, j) = \frac{length(i,j)}{length(i,j)+avg(length)}$, η is used to balancing angle and edge energy, normally 0.5.

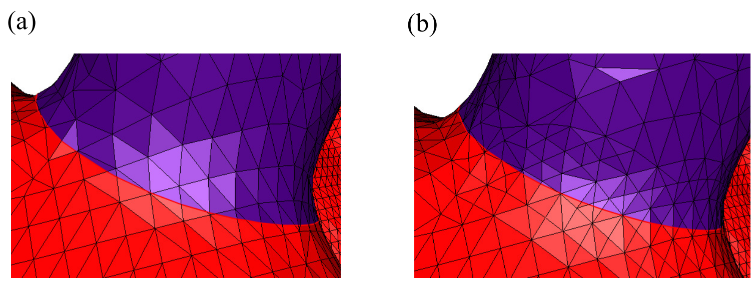

Figure 7: Comparison diagram before and after optimization. **a**:Before optimization; **b**:After optimization.

As shown in Fig.7, after the segmentation boundary optimization, the segmented sub-mesh boundary will be smoother and the segmentation boundary will fit the original isoline better.

4. Experimental results and discussion

In this section, we present experimental results obtained on the triangulated mesh models, which mainly come from the Princeton shape Benchmark database. The experimental hardware platform of the proposed algorithm is a notebook computer, equipped with AMD Ryzen 7 4800u 2.10 GHz six core processor and 16GB RAM.

Table 1: The parametersthe of generated isoline lines by strokes of users

Isoline	Contour radius	Central index	Isoline local index	Final evaluation index
line 1	0.329619	0.686908	0.069181	0.0475209
line 2	0.291536	0.764228	0.0145211	0.0110974
line 3	0.263238	0.83527	-0.0125843	-0.0105113
line 4	0.241766	0.89683	-0.0218866	-0.0196285
line 5	0.224106	0.945959	-0.0251432	-0.0237845
line 6	0.209203	0.9801994	-0.0290432	-0.0284681
line 7	0.197797	0.99778	-0.0343168	-0.0342406
line 8	**0.191638**	**0.99778**	**-0.0376692**	**-0.0375856**
line 9	0.192596	0.980199	-0.0334415	-0.0327793
line10	0.199868	0.9459594	-0.0206012	-0.0194879
line 11	0.210924	0.89683	0.00189612	0.00170049
line 12	0.223829	0.83527	0.0407296	0.0340203
line 13	0.237291	0.764228	0.104099	0.0795552

∗The best results are bold.

4.1. Isoline selection experiment

In this experiment, the 161st bear model in the data set was selected, including 13826 points and 27648 faces. We draw a line between the bear's head and body to segment the head and body and obtain the details of 13 isoline lines, as shown in Table 1.

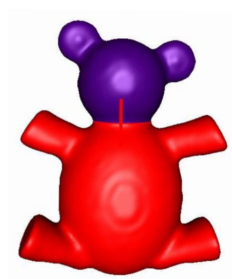

Figure 8: The Segmentation results of bear model based on the 8th segmentation line.

According to the section Isoline selection definition, the M_i smallest isoline is determined as the best optimal segmentation path, so we choose the 8th segmentation line, and the obtained segmentation result is shown in Fig.8. Fig.9 presents the segmentation results of our method on the basis of isoline selection experiment, we extract the two segmented parts. The head has 1598 vertices and 7133 faces and the body has 10288 vertices and 20394 faces.

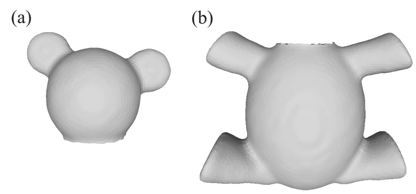

Figure 9: The segmentation results of our method on the basis of isoline selection experiment.**a**:The segmented head of bear model;**b**:The segmented body of bear model.

Figure 10: The results of multi-component segmentation.

Furthermore, the experiments have been carried out on a variety of mesh models in this section. The segmentation effect is excellent. The user segmentation intent is accurately identified and the segmentation isoline across the boundary is formed. The results of multi-component segmentation and binary segmentation are shown in Fig.10 and Fig.11 respectively.

4.2. Boundary optimization

An encrypted boundary optimization algorithm was introduced on the basis of isoline selection. The increased mesh vertices and patches after optimization are concentrated at the encrypted segmentation boundaries, and the contrast results are displayed in Fig.12. The experimental results show that the segmented boundary is more fine-grained, and the boundary fits the curved feature better.

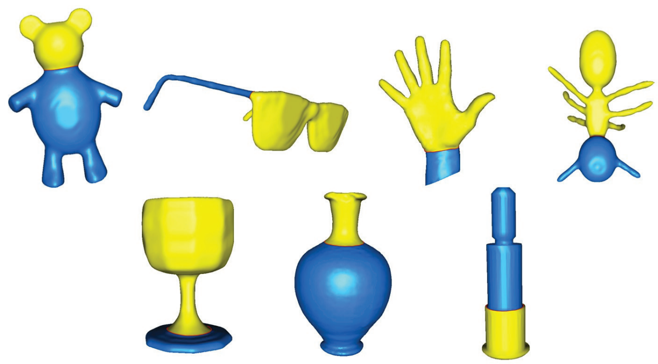

Figure 11: The results of binary segmentation.

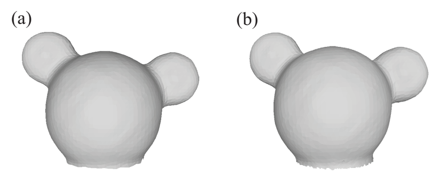

Figure 12: Comparison of boundary optimization, the right figure shows the optimized result.

4.3. Comparison and Evaluation

To verify the effectiveness of the proposed method, several experiments and quantitatively assessment are conducted to illustrate the effectiveness of the proposed method. In comparative experiments, our proposed semi-automatic segmentation method based on the harmonic field exhibits good adaptability, combining the user's intention and the actual geometry to obtain good results. But it is still notable that the user's strokes are required to be long enough to generate enough isolines to select the final segmentation isolines, however, this operation is difficult to perform in complex or feature-adjacent regions. Fig.13 and Fig.14 demonstrate comparison of segmentation results with two other methods.

Besides the subjective visual comparison, we also carry out quantitative comparison. We use the evaluation measures proposed by Chen et al. [36]to quantitate the segmentation results.The specific indicators contain segmentation difference, Hamming distance, Rand index, and consistency error. Each of these metrics is specified as follows:

Figure 13: Comparison of segmentation results with two other methods. Results in the first and second column are inner dihedral angle and spectral clustering respectively, the last column represent our segmentation results.

Figure 14: Comparison of segmentation results with two other methods on human model. Results in the third column represent our segmentation results.

Segmentation difference: It is used to calculate the discrepancy of segmentation paths on the mesh. For two segmentations S_1 and S_2, the point sets of the segmentation paths are C_1 and C_2, respectively, and the segmentation difference is:

$$\mathrm{CD}(\mathrm{S_1}, \mathrm{S_2}) = \frac{\mathrm{mean}\{d_G(p_1, C_2)\} + \mathrm{mean}\{d_G(p_2, C_1)\}}{avgRadius} \tag{12}$$

$\forall p_1 \in C_1, \forall p_2 \in C_2,$

$$d_G(p_1, C_2) = \min\{d_G(p_1, p_2), \forall p_2 \in C_2\} \tag{13}$$

$$d_G(p_2, C_1) = \min\{d_G(p_2, p_1), \forall p_1 \in C_1\} \tag{14}$$

where $d_G(p_1, C_2)$ is the geodesic distance from point $p_1 \in C_1$ to C_2, $d_G(p_2, C_1)$ is the geodesic distance from point $p_2 \in C_2$ to C_1, mean is the mean value, and $agvRadius$ is the average Euclidean distance from the point to the model center of mass.

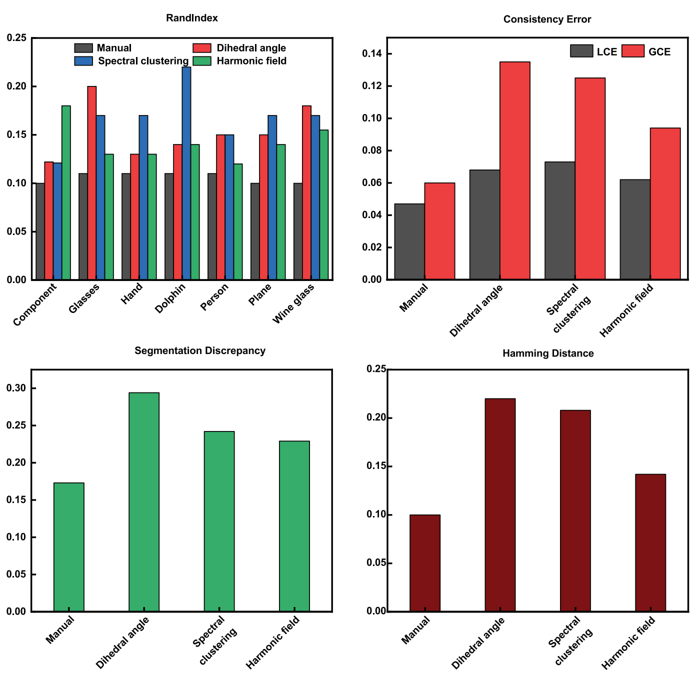

Figure 15: The quantitative comparison evaluation of the proposed method, the last column represent our segmentation method.

Hamming distance: It is used to calculate the difference between the two segmentations S_1, S_2, which is expressed as:

$$\mathrm{HD}(\mathrm{S_1}, \mathrm{S_2}) = \frac{1}{2}\left(\frac{D_H(S_1 \Rightarrow S_2)}{\|S\|} + \frac{D_H(S_2 \Rightarrow S_1)}{\|S\|}\right) \tag{15}$$

where $D_H(S_1 \Rightarrow S_2) = \sum_i \|S_2^i \setminus S_1^{it}\|, \setminus$ is the set of difference operators.

Rand index: used to measure whether faces p and q belong to the same partition, which is defined as:

$$\mathrm{RI} = 1 - \binom{2}{N}^{-1} \sum_{p,q,p<q} [B_{pq}P_{pq} + (1 - B_{pq})(1 - P_{pq})] \tag{16}$$

where N is the number of faces, $B_{pq}P_{pq} = 1$ indicates that two faces belong to the same partition in both methods, and $(1 - B_{pq})(1 - P_{pq})$ indicates that two faces do not belong to the same partition in both methods.

Consistency error: It includes two types of local and globalwhich are used to determine the similarity and dissimilarity of the nested or hierarchical structure in partition S_1 and S_2, local is $LCE(S_1, S_2)$ and global is $GCE(S_1, S_2)$:

$$\mathrm{LCE}(\mathrm{S}_1, \mathrm{S}_2) = \frac{1}{n} \sum_i \min\{\frac{\|R(S_1, f_i) \setminus R(S_2, f_i))\|}{\|R(S_1, f_i)\|}, \frac{\|R(S_2, f_i) \setminus R(S_1, f_i)\|}{\|R(S_2, f_i)\|}\} \tag{17}$$

$$\mathrm{GCE}(\mathrm{S}_1, \mathrm{S}_2) = \frac{1}{n} \min\{\sum_i \frac{\|R(S_1, f_i) \setminus R(S_2, f_i))\|}{\|R(S_1, f_i)\|}, \sum_i \frac{\|R(S_2, f_i) \setminus R(S_1, f_i)\|}{\|R(S_2, f_i)\|}\} \tag{18}$$

where $R(S_1, f_i)$is a set of connected faces of the segmented region.

Fig.15 shows the quantitative comparison results on several models which come from the Princeton shape benchmark database of our method compared with other segmentation methods, including Manual, Dihedral angle and Spectral clustering.

The metric (Cut Discrepancy) is boundary-based, and the last three metric (Hamming Distance, Rand Index, Consistency Error) are region-based. These four metrics are used to evaluate the similarity between segmentation results generated by different methods with human-generated ones. The quantitative evaluation results and the visual segmentation results demonstrate that our method can achieve the visually meaningful segmentation results, especially for a specific semantic component (such as the head, extremities and tail) according to the needs of users.

5. Conclusion

In this paper, we propose a semi-automatic interactive 3D mesh segmentation method based on stroke-constrain. We use the harmonic field as the mesh metric, a smooth harmonic field is introduced based on Laplace operator and Poisson equation. With carefully selected of weight, the generated harmonic field is more suitable for the geometric characteristics of the mesh itself, and the user strokes are used as constraints to seek a set of contour lines, and the most suitable contour line is selected as the segmentation path, finally the segmentation path is optimized to obtain the segmented sub-graph. The experiment of this method proves that the semi-automatic mesh segmentation can fully understand the user's intention, combining the mesh information and the intuitive principle of minimum negative curvature to achieve visually meaningful segmentation.

Declarations

- Funding

  This work was supported by Beijing Natural Science Foundation and Fengtai Rail Transit Frontier Research Joint Fund (No. L191009), the National Natural Science Foundation of China (No. 61877002, 62277001), Scientific Research Program of Beijing Municipal Education Commission No. KZ202110011017.

- Conflict of interest

  The authors declare that they have no conflict of interest.

- Ethics approval Not applicable
- Consent to participate Not applicable
- Consent for publication Not applicable
- Availability of data and materials Not applicable
- Code availability Not applicable
- Authors' contributions

  All authors contributed to the study conception and design. Haisheng Li and Nan Li provide the methodology. The first draft of the manuscript was written by Jiguang Lian and Xiaochuan Wang. All authors commented on previous versions of the manuscript. All authors read and approved the final manuscript.

References

[1] P. V. Sander, Z. J. Wood, S. Gortler, J. Snyder, H. Hoppe, Multi-chart geometry images (2003).

[2] P. V. Sander, J. Snyder, S. J. Gortler, H. Hoppe, Texture mapping progressive meshes, in: Proceedings of the 28th annual conference on Computer graphics and interactive techniques, 2001, pp. 409–416.

[3] H. Li, Y. Zheng, X. Wu, Q. Cai, 3d model generation and reconstruction using conditional generative adversarial network, International Journal of Computational Intelligence Systems 12 (2019) 697.

[4] Q. Yuan, G. Li, K. Xu, X. Chen, H. Huang, Space-time co-segmentation of articulated point cloud sequences, in: Computer Graphics Forum, volume 35, Wiley Online Library, 2016, pp. 419–429.

[5] A. Sheffer, E. Praun, K. Rose, et al., Mesh parameterization methods and their applications, Foundations and Trends® in Computer Graphics and Vision 2 (2007) 105–171.

[6] K. Zhou, J. Synder, B. Guo, H.-Y. Shum, Iso-charts: stretch-driven mesh parameterization using spectral analysis, in: Proceedings of the 2004 Eurographics/ACM SIGGRAPH symposium on Geometry processing, 2004, pp. 45–54.

[7] H. Li, T. Zhao, N. Li, Q. Cai, J. Du, Feature matching of multi-view 3d models based on hash binary encoding, Neural Network World 27 (2017) 95.

[8] S. Shlafman, A. Tal, S. Katz, Metamorphosis of polyhedral surfaces using decomposition, in: Computer graphics forum, volume 21, Wiley Online Library, 2002, pp. 219–228.

[9] M. Zöckler, D. Stalling, H.-C. Hege, Fast and intuitive generation of geometric shape transitions, The Visual Computer 16 (2000) 241–253.

[10] H. Li, Y. Zheng, J. Cao, Q. Cai, Multi-view-based siamese convolutional neural network for 3d object retrieval, Computers and Electrical Engineering 78 (2019) 11–21.

[11] H. Li, L. Sun, S. Dong, X. Zhu, Q. Cai, J. Du, Efficient 3d object retrieval based on compact views and hamming embedding, IEEE Access 6 (2018) 31854–31861.

[12] H. LI, X. LIU, L. LAI, Q. CAI, J. DU, An area weighted surface sampling method for 3d model retrieval, Chinese Journal of Electronics 23 (2014) 484–488.

[13] E. Zuckerberger, A. Tal, S. Shlafman, Polyhedral surface decomposition with applications, Computers & Graphics 26 (2002) 733–743.

[14] A. Shamir, A survey on mesh segmentation techniques, in: Computer graphics forum, volume 27, Wiley Online Library, 2008, pp. 1539–1556.

[15] E. Zhang, K. Mischaikow, G. Turk, Feature-based surface parameterization and texture mapping, ACM Transactions on Graphics (TOG) 24 (2005) 1–27.

[16] S. Katz, A. Tal, Hierarchical mesh decomposition using fuzzy clustering and cuts, ACM transactions on graphics (TOG) 22 (2003) 954–961.

[17] J.-M. Lien, J. Keyser, N. M. Amato, Simultaneous shape decomposition and skeletonization, in: Proceedings of the 2006 ACM symposium on Solid and physical modeling, 2006, pp. 219–228.

[18] J. Zhang, J. Zheng, C. Wu, J. Cai, Variational mesh decomposition, ACM Transactions on Graphics (TOG) 31 (2012) 1–14.

[19] Y. Lee, S. Lee, A. Shamir, D. Cohen-Or, H.-P. Seidel, Intelligent mesh scissoring using 3d snakes, in: 12th Pacific Conference on Computer Graphics and Applications, 2004. PG 2004. Proceedings., IEEE, 2004, pp. 279–287.

[20] Y. Lee, S. Lee, A. Shamir, D. Cohen-Or, H.-P. Seidel, Mesh scissoring with minima rule and part salience, Computer Aided Geometric Design 22 (2005) 444–465.

[21] Y. Hou, Y. Zhao, A robust segmentation algorithmfor for 3d complex meshes, in: Journal of Physics: Conference Series, volume 1802, IOP Publishing, 2021, p. 032045.

[22] A. Khosravanian, M. Rahmanimanesh, P. Keshavarzi, S. Mozaffari, Fuzzy local intensity clustering (flic) model for automatic medical image segmentation, The Visual Computer 37 (2021) 1185–1206.

[23] G. Zeng, H. Li, X. Wang, N. Li, Point cloud up-sampling network with multi-level spatial local feature aggregation, Computers & Electrical Engineering 94 (2021) 107337.

[24] X. Chen, S. Jiang, L. Guo, Z. Chen, C. Zhang, Whole brain segmentation method from 2.5 d brain mri slice image based on triple u-net, The Visual Computer (2021) 1–12.

[25] J. H, G. G, Z. M, Z. J, Watershed 3d mesh segmentation based on regional discrete curvature, Computer Engineering and Applications 51 (2015) 182–186.

[26] M. Garland, A. Willmott, P. S. Heckbert, Hierarchical face clustering on polygonal surfaces, in: Proceedings of the 2001 symposium on Interactive 3D graphics, 2001, pp. 49–58.

[27] J. Lian, H. Li, N. Li, Q. Cai, An adaptive mesh segmentation via iterative k-means clustering, in: Proceedings of 2021 Chinese Intelligent Systems Conference, Springer, 2022, pp. 193–201.

[28] D. Cohen-Steiner, P. Alliez, M. Desbrun, Variational shape approximation, in: ACM SIGGRAPH 2004 Papers, 2004, pp. 905–914.

[29] Y. Fang, M. Sun, M. Kim, K. Ramani, Heat-mapping: A robust approach toward perceptually consistent mesh segmentation, in: CVPR 2011, IEEE, 2011, pp. 2145–2152.

[30] X. Yang, M. Su, X. Han, A wave kernel segmentation algorithm based on persistence clustering, Modern Electronics Technique 23 (2019) 135–140. doi:https://doi.org/10.16652/j.issn.1004-373x.2019.23.029.

[31] H. Wang, T. Lu, O. K.-C. Au, C.-L. Tai, Spectral 3d mesh segmentation with a novel single segmentation field, Graphical models 76 (2014) 440–456. doi:https://doi.org/10.1016/j.gmod.2014.04.009.

[32] M. Chahhou, L. Moumoun, M. El Far, T. Gadi, Segmentation of 3d meshes usingp-spectral clustering, IEEE transactions

on pattern analysis and machine intelligence 36 (2014) 1687–1693. doi:https://doi.org/10.1109/TPAMI.2013.2297314.

[33] L. L.-j. YANG Jun, TIAN Zhen-hua, W. Xiao-peng, Segmentation of 3d geometric models based on mesh laplace, Computer Science 42 (2015) 295–299. doi:https://doi.org/10.1109/TPAMI.2013.2297314.

[34] W. Tong, X. Yang, M. Pan, F. Chen, Spectral mesh segmentation via gradient minimization, IEEE Transactions on Visualization and Computer Graphics 26 (2018) 1807–1820.

[35] J.-H. Moon, S. Park, S.-H. Yoon, 3d magic wand: Interface for mesh segmentation using harmonic field, Journal of the Korea Computer Graphics Society 28 (2022) 11–19.

[36] X. Chen, A. Golovinskiy, T. Funkhouser, A benchmark for 3d mesh segmentation, Acm transactions on graphics (tog) 28 (2009) 1–12. doi:https://doi.org/10.1145/1531326.1531379.